Atomic layer deposition enabled MgO surface coating on porous TiO$_2$ for improved CO$_2$ photoreduction

Xuhui Feng[a], Fuping Pan[a], Huilei Zhao[a], Wei Deng[a], Peng Zhang[b], Hong-Cai Zhou[b,c], Ying Li[a,*]

[a] Department of Mechanical Engineering, Texas A&M University, College Station, TX 77843, USA
[b] Department of Chemistry, Texas A&M University, College Station, TX 77840, USA
[c] Department of Materials Science and Engineering, Texas A&M University, College Station, TX 77840, USA

ARTICLE INFO

ABSTRACT

In this work, we have prepared porous TiO$_2$ with mixed anatase-rutile phases from a metal-organic framework MIL-125 and employed atomic layer deposition (ALD) method to coat an ultrathin MgO overlayer on porous-TiO$_2$. The CO$_2$ photoreduction performance of porous-TiO$_2$ was more than 4 times higher than that of commercial Degussa P25. The MgO coating on porous-TiO$_2$ by ALD in the range of 1 to 100 atomic layers all improved CO$_2$ photoreduction performance, with 5 layers of MgO being the optimal, delivering 4 times higher CO production than that by pristine porous-TiO$_2$ and 21 times higher than P25. It is demonstrated that the uniform dispersion of MgO on TiO$_2$ surface led to increased concentration of surface Ti^{3+} species and Mg bonded hydroxyl groups, which are active sites for CO$_2$ adsorption and photoreduction. The ALD layer also served to passivate the TiO$_2$ surface states and hinder surface electron-hole recombination. In addition, a conventional wet-impregnation (WI) method was applied to incorporate MgO on porous-TiO$_2$ to serve as a comparison. The WI modified MgO/TiO$_2$ samples were more active than pristine porous-TiO$_2$ but less active than ALD modified MgO/TiO$_2$, because the ALD samples presented significantly higher amounts of surface Ti^{3+} than WI samples due to higher and more uniform MgO surface coverage by ALD coating. Findings from this original work on ALD modification to enhance photocatalytic performance may be extended to other photocatalyst systems and other catalytic reactions.

1. Introduction

The greenhouse effect, originated from rising of atmospheric CO$_2$ level, is one of the most concerning topics in the 21st century. As one of the available techniques to tackle this issue, CO$_2$ reduction processes, which convert CO$_2$ molecules into clean fuels and value-added chemicals (CO, CH$_4$, methanol, formic acid, etc.), have been highlighted among available approaches [1,2]. However, due to the stable nature of CO$_2$ molecules, high energy input and high temperature/pressure are normally required to activate the reactants in CO$_2$ reduction process [3]. Photocatalytic process, which utilizes free and abundant solar energy to activate chemical reactions under mild reaction conditions, is a potential method for cost-effective CO$_2$ conversion into value-added chemicals [4–6]. Up to now, a variety of photocatalyst materials such as TiO$_2$ [7–10], BiOCl [11], ZrO$_2$ [12] and metal-organic frameworks [13,14] have been reported for applications in CO$_2$ photoreduction processes. Among the wide range of available photocatalysts, TiO$_2$ is the most studied for CO$_2$ photoreduction because of its merits including

chemical stability, nontoxicity, high oxidizing power, low-cost as well as abundant supply [15–17]. However, many drawbacks of TiO$_2$, such as (1) wide band gap (3.0 eV for rutile and 3.2 eV for anatase), (2) fast recombination of photo-induced holes and electrons, and (3) limited CO$_2$ adsorption capacity, restrict photoactivity of TiO$_2$ and narrow the applications of TiO$_2$ in photocatalytic CO$_2$ reduction [4,15,18].

One effective approach to improve the CO$_2$ photoreduction performance of TiO$_2$ is to prepare high surface area TiO$_2$ to enhance CO$_2$ adsorption and generates more active sites for desired reaction [8,19]. Metal-organic framework (MOF) materials, which exhibit very high surface area and tunable framework structure [20], have recently demonstrated their applicability as appropriate precursor to prepare porous metal oxide with high surface area and hierarchical porous structure [21,22]. Recently, porous TiO$_2$ derived from metal-organic framework MIL-125 has drawn many attentions due to the favorable hierarchical porous structure and high surface area. According to previous reports, MIL-125 derived porous TiO$_2$ exhibits high surface area ranging from 125 m^2/g to 220 m^2/g [23,24]. Due to those favorable

properties, MIL-125 derived porous TiO_2 has been reported in photocatalytic applications such as hydrogen production [24], ammonia gas degradation [25], water splitting [26] and methylene blue degradation [27]. Up to now, to our best of knowledge, though the MIL-125 derived porous TiO_2 exhibit many favorable properties, its application in CO_2 photoreduction has not been reported. Herein, we report the application of porous hierarchical TiO_2 derived from MIL-125 for the first time in CO_2 photoreduction.

Besides the preparation of porous TiO_2, the incorporation of noble metals (e.g., Pt, Pd, Ru, and Ag) [24,28,29] or low-cost metal oxides (e.g. Fe_2O_3 [30], NiO [31], and CuO [32]) have been demonstrated for their potential in effectively promoting photocatalytic activity by hindering the charge recombination, enhancing visible light absorption, and altering surface states or defects [33–35]. Previous studies [36–40] demonstrated the role of MgO in boosting CO_2 photoreaction performance by decreasing electron-hole recombination and promoting adsorption of CO_2 because of the basic nature of MgO. Conventional approaches of TiO_2 surface modification includes wet impregnation (WI) [36,37] and ultrasonic spray pyrolysis (USP) [37], which are easy and economical ways for surface modification of TiO_2. However, those methods produce segregated, irregular-shape islands or patches of MgO deposited on TiO_2 without full coverage of the TiO_2 surface. In order to take the advantage of porous, high surface area TiO_2, it is desirable to incorporate more uniformly distributed MgO on TiO_2 with maximized contact between the two species. The recently emerged atomic layer deposition (ALD) technique, compared with conventional methods, allows easy yet precise control on the growth and thickness of multilayer deposition structure, and thus is a desirable way to coat uniform thin films [16]. To the best of our knowledge, no work has been investigated on TiO_2 modified by ALD coated MgO overlayer for CO_2 photoreduction. Furthermore, despite that MgO is cheap, nontoxic and naturally abundant, only a limited number of studies are reported on MgO modified TiO_2 for CO_2 photoreduction [36,37,41], and the effect of MgO nanostructure on CO_2 photoreduction is not fully understood.

The objective of this work was to synthesize porous, high surface area TiO_2 derived from metal-organic framework MIL-125 and modify the surface with uniformly dispersed MgO to improve the efficiency of photocatalytic CO_2 reduction. Based on the aforementioned literature review, we hypothesize that porous TiO_2 is superior to traditional nanopowder photocatalysts such as P25 and that MgO coated on TiO_2 surface through the ALD method is advantageous over non-modified TiO_2 or MgO modified TiO_2 by traditional methods such as wet impregnation. In this work, porous TiO_2, ALD and WI modified porous TiO_2 photocatalysts were prepared and compared in terms of surface morphology, optical properties, surface chemical states as well as CO_2 photoreduction activity. The advantages of ALD as an enabling technique for fabricating efficient CO_2 photoreduction catalysts were elucidated.

2. Experimental

2.1. Preparation of MIL-125

MIL-125 was prepared based on a previously reported method [23,24]. In a typical experiment, 6.0 g of terephthalic acid ($C_8H_6O_4$, > 99.0%, Tokyo Chemical Industry) was dissolved in a solvent mixture prepared with 108 ml of *N,N*-dimethylformamide (DMF, C_3H_7NO, ≥ 99.8%, BDH Chemicals) and 12 ml of methanol (C_2H_6O, ≥ 99.8%, EMD Millipore). 3.12 ml of titanium tetraisopropoxide (TTIP, $TiC_{12}H_{28}O_4$, 97 + %, Alfa Aesar) was added into the solution under stirring. The mixture was then transferred into a Teflon lined autoclave. The autoclave was placed in a conventional oven and maintained at 150 °C for 24 h. After hydrothermal treatment, white powder was collected by centrifugation. The powder was rinsed with methanol for three times before drying in a vacuum oven at 80 °C overnight, yielding MIL-125.

2.2. Preparation of porous-TiO_2

Porous-TiO_2 was prepared using MIL-125 as a template. In a typical preparation, MIL-125 powder was firstly pyrolyzed in a tube furnace at 500 °C for 2 h under argon atmosphere, and the resultant black powder was then calcined in air at 450 °C for 2 h to obtain white TiO_2 powder.

2.3. Wet impregnation (WI) of MgO on porous-TiO_2

In a typical preparation, 100 mg of porous-TiO_2 was mixed with 40 ml of $Mg(NO_3)_2$ (99%, Sigma-Aldrich) aqueous solution at a certain concentration. The mixture was stirred at room temperature for 24 h and then dried in vacuum at 80 °C overnight. The white powder was then collected and calcined at 450 °C in air for 2 h. The obtained samples are denoted as x%WI, where x% indicates the weight percentage of Mg^{2+} against porous-TiO_2 in the recipe.

2.4. Atomic layer deposition (ALD) of MgO overlayer on porous-TiO_2

An Ultratech Savannah S200 ALD system was used to coat a MgO overlayer on porous-TiO_2. A homemade powder holder loaded with 30 mg of porous-TiO_2 powder was placed in the center of ALD chamber, which was maintained at 200 °C during the ALD process. Bis(ethylcyclopentadienyl) magnesium $[Mg(C_5H_4C_2H_5)_2$, min. 98%, Strem Chemicals Inc.] was used as the Mg precursor. In each ALD cycle, "expo mode" was used for coating porous materials, and the pulse time of water and Mg precursor was set to 2 s each to introduce adequate amount of reactants to the reaction chamber and ensure even ALD coating on porous-TiO_2. After the ALD process, a grey powder was obtained and calcined at 450 °C for 30 min to remove any potential organic residues from the ALD process. A white powder was eventually obtained. The ALD samples are denoted as xALD, where x is the number of ALD cycle applied on porous-TiO_2.

2.5. Photocatalyst characterization

X-ray diffraction (XRD) analysis was performed on a Bruker-AXS D8 Advance diffractometer using Cu Kα1 irradiation (λ = 1.54059 Å) at 40 kV and 40 mA at room temperature. The step increment was set at $2\theta = 0.05°$ and the counting time per step was 1 s. The morphology, structure were analyzed with a JEOL JSM7500 F field-emission scanning electron microscope (FE-SEM) and a FEI Tecnai G2 F20 ST transmission electron microscope (TEM). UV–vis diffuse reflectance spectra were measured on a Hitachi U4100 UV–vis-NIR Spectrophotometer with Praying Mantis accessory. Brunauer-Emmett-Teller (BET) surface area analysis was performed on a Micromeritics ASAP 2420 physisorption analyzer. Prior to surface area measurements, the photocatalyst samples were degassed in vacuum at 100 °C for 12 h. X-ray photoelectron spectroscopy (XPS) analysis was performed on an Omicron XPS system. Photoluminescence spectra (PTI QuantaMaster series Spectrofluorometer) were obtained to investigate the charge recombination emission using 300 nm incident light, scanning from 400 to 600 nm with scan rate 0.1 nm/s. Transient photocurrents of the prepared samples were measured with a Gamry Reference 3000 potentiostat. 1.2 mg of sample was loaded on the conductive surface of an ITO glass and a 0.05 M Na_2SO_4 solution was used as electrolyte. The same 450 W Xe lamp used in CO_2 photoreduction test was employed as light source, a 3 M Ag/AgCl electrode was used as the reference, and a Pt slice was used as counter electrode.

2.6. CO_2 photoreduction performance test

The experimental setup for CO_2 photoreduction was similar to that in our previous report [16]. A piece of glass fiber filter paper (Pall Corporation) was used as the support for powder photocatalyst. Prior to catalyst loading, the glass fiber paper was calcined in air at 450 °C to

remove organics on the surface, if any. Then, 10 mg of photocatalyst was dispersed in 2 ml of de-ionized water and sonicated for 10 min. The obtained suspension was dropped onto the glass fiber paper, which was later dried in vacuum oven at 80 °C for 30 min. The catalyst-loaded glass fiber paper was then placed into a tubular quartz reactor with photocatalyst side facing the light source. Ultra-high purity CO_2 (99.999%, Airgas) was bubbled into a water reservoir to generate a CO_2/H_2O gas mixture (water vapor concentration $\approx$ 2.3% by volume) before purged into the tube reactor. Before turning the light on, the system was flushed at a CO_2 flow rate of 298.0 standard cubic centimeter per minute (sccm) for 1 h and then maintained at 3.0 sccm. Light source used in this study was a 450 W Xe lamp (Newport, Inc.) equipped with a water filter to diminish infrared irradiation, the distance between the Xe lamp and the photocatalyst was 30 cm. The light spectrum of the lamp measured 30 cm away from the lamp is shown in Fig. S1 (Supporting information). Intensity of UV, visible, IR light of the Xe lamp measured with/without the quartz tube is listed in Table S1. The outlet of the reactor was connected with a Shimadzu GC-2014ATF gas chromatograph, which was equipped with an autosampler, a thermal conductivity detector (TCD, to detect H_2, O_2, and CO_2 when applicable), and a flame ionization detector (FID) coupled with a methanizer (to detect CO and CH_4 when applicable).

3. Result and discussion

3.1. Crystal structure

Fig. S2 shows the XRD pattern of as synthesized MIL-125 powder, which is a titanium based MOF and used as the precursor of porous-TiO_2. The sharp peaks in the XRD pattern confirm high crystallinity of the as prepared MIL-125 sample, which also agree with the XRD patterns of MIL-125 reported in the literature [42]. SEM image of as prepared MIL-125 (Fig. S3) illustrates the well defined dish-like shape of the sample.

The XRD patterns of all prepared photocatalyst are shown in Fig. 1. It was found that all samples are consist of both anatase and rutile phases. The existence of rutile phase is possibly a result of anatase to rutile phase change induced by elevated pyrolysis temperature in porous-TiO_2 preparation. Weight ratio of anatase/rutile was calculated by Rietveld refinement method [43]. Phase composition and crystallite size of anatase and rutile in the three representative samples are listed in Table 1. The prepared samples show a comparable phase composition made of anatase and rutile. WI and ALD samples had a slightly higher rutile phase and a slightly larger rutile crystallite size than

Fig. 1. XRD patterns of (a) porous-TiO₂, (b) 0.1%WI, (c) 0.5%WI, (d) 1%WI, (e) 2%WI, (f) 5%WI, (g) 10%WI, (h) 1ALD, (i) 2ALD, (j) 5ALD, (k) 10ALD, (l) 20ALD, (m) 50ALD, (n) 100ALD.

Table 1
Phase composition and crystallite size of prepared samples.

| Sample ID	Anatase %	Rutile %	Anatase Crystallite Size (nm)	Rutile Crystallite Size (nm)
porous-TiO₂	43.9	56.1	11.3	13.9
0.1%WI	39.2	60.8	14.0	16.1
0.5%WI	39.5	60.5	12.2	15.5
1%WI	39.2	60.8	12.1	15.1
2%WI	40.2	59.8	12.6	15.0
5%WI	39.8	61.2	11.0	14.9
10%WI	33.7	66.3	12.7	15.5
1ALD	39.4	60.6	13.4	14.8
2ALD	39.4	61.6	12.7	15.2
5ALD	39.0	61.0	12.1	14.8
10ALD	38.8	61.2	11.9	14.2
20ALD	39.1	60.9	12.8	14.7
50ALD	39.2	60.8	12.2	15.4
100ALD	49.8	50.2	11.6	15.5

porous-TiO_2, probably due to the extended thermal treatment processes undergone on those samples. For most samples, diffraction peaks for MgO were not found, likely due to the small weight percentage of MgO and its good dispersion on porous-TiO_2. The exception is 100ALD, where the existence of MgO was confirmed by the characteristic peak of MgO at 2θ = 42.9°. With 100 layers of MgO addition, the MgO loading amount was considerably higher than other samples and detectable by XRD.

3.2. Morphology

The morphologies of porous-TiO_2, 2%WI and 5ALD are shown in SEM images in Fig. 2. porous-TiO_2 particles exhibit a cubic shape with an average particle size of ~270 nm (Fig. 2a). Compared with porous-TiO_2, 2%WI (Fig. 2d) and 5ALD (Fig. 2g) have a similar particle size, but the surface of 2%WI sample has a considerable level of roughness and irregular agglomeration of ultrafine particles. In the preparation procedure of WI samples, $Mg(NO_3)_2$ was firstly crystalized on the surface of porous-TiO_2 nanoparticles after the evaporation of $Mg(NO_3)_2$ solution. The surface $Mg(NO_3)_2$ deposition was then converted to MgO nanoparticles during the subsequent calcination process, which likely resulted in the elevated surface roughness and irregularity [41,44]. In contrast, 5ALD (Fig. 2g) has a smooth surface similar to porous-TiO_2, in coincident with the morphology of coating. In addition, shown in Fig. 2g, the SEM image of 5ALD is blurry, which is likely due to the reduced surface conductivity of the photocatalyst caused by the MgO overlayer. Since MgO is an insulator, the reduction in conductivity indicates successful coating of MgO overlayer on the porous-TiO_2.

TEM analyses were performed on porous-TiO_2, 2%WI and 5ALD to further investigate the morphology and crystal structure of the photocatalysts (Fig. 2b, c, e, f, h, i). As shown in Fig. 2b, porous-TiO_2 particles have an average size of ~270 nm, consisting of firmly interconnected ultrafine nanoparticles, with distinct pore structure. Similar morphology was observed for 5ALD and 2%WI. However, 2%WI exhibited a relatively loosened nanoparticle packing, compared to porous-TiO_2 and 5ALD, which coincides with the relatively higher surface roughness observed in the 2%WI SEM image. As displayed in Fig. 2c, f, i, both anatase phase (d = 0.352 nm) and rutile phase (d = 0.323 nm) were found on porous-TiO_2, 2%WI, and 5ALD samples, agreeing with the XRD results. However, due to the low amount of MgO addition on 2%WI and 5ALD samples, characteristic lattice of MgO was not observed.

TEM analysis on 100ALD was also performed to probe the morphology and crystal structure of MgO at a higher loading level (Fig. S4). A lattice spacing at d = 0.21 nm was identified that corresponds to crystalline MgO. This result also agrees with the XRD data of 100ALD sample (Fig. 1n), where MgO diffraction peak was seen. Interestingly, instead of being a uniform overcoating layer, the ALD added MgO was
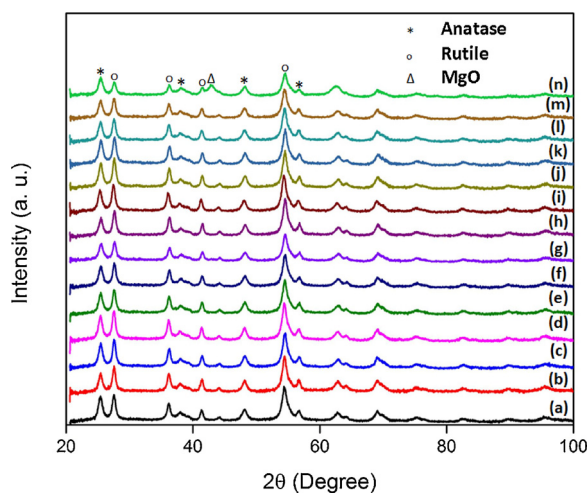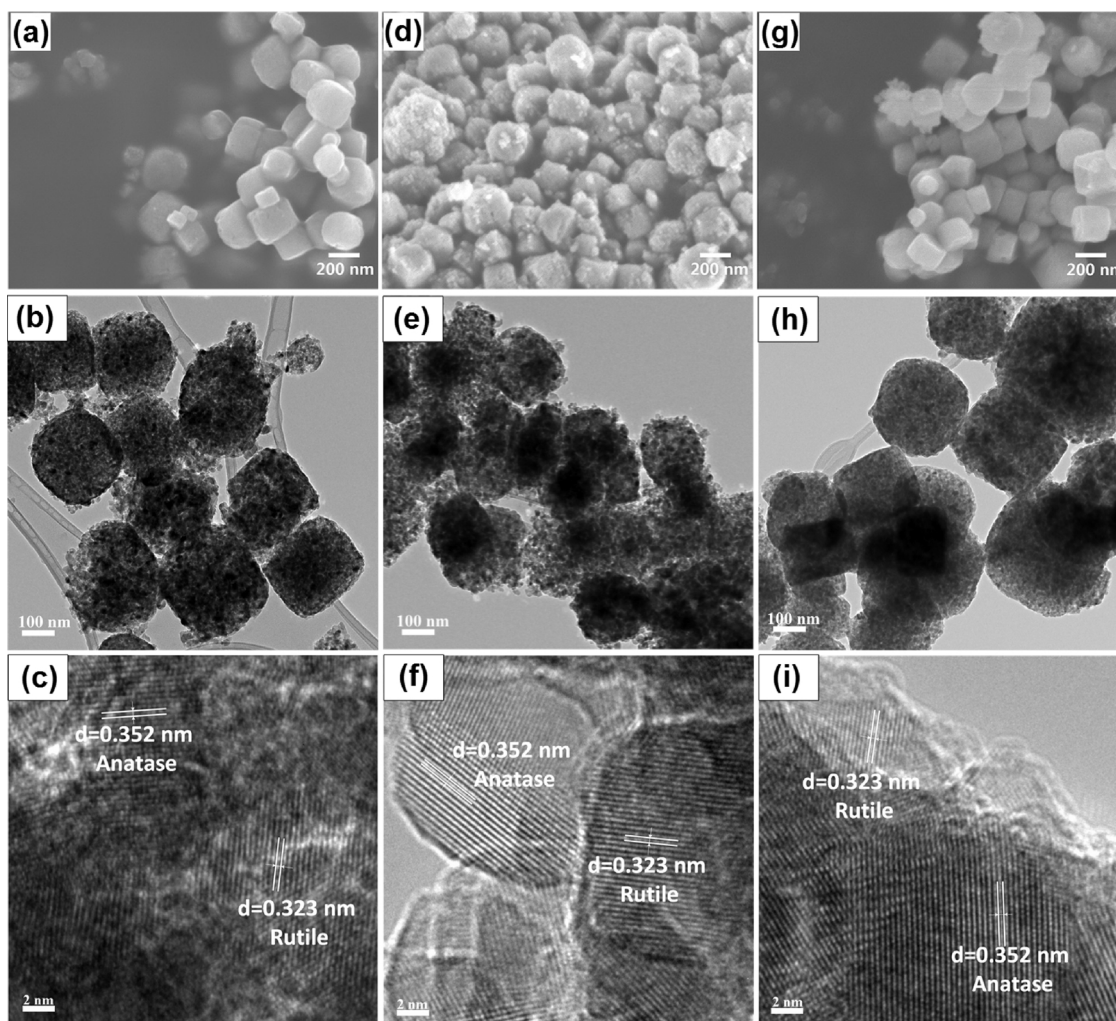
Fig. 2. SEM and TEM images of (a–c) porous-TiO$_2$, (d–f) 2%WI, and (g–i) 5ALD samples.

found in the form of nanoparticle deposition on 100ALD. As mentioned in the catalyst preparation section, all ALD prepared samples were calcined in air at 450 °C after ALD treatment to eliminate any potential organic residue from ALD process. Thus, it is highly likely that MgO as thick as 100 ALD layers sintered during the calcination process and turned into fine nanoparticles deposited on the surface of the photocatalyst. Nonetheless, for 5ALD sample, as the ALD coated layer was ultrathin, sintering effect of MgO was not observed (Fig. 2g, h, i).

3.3. Porous structure

In order to evaluate porosity of as prepared photocatalysts in this study, Brunauer–Emmett–Teller (BET) analysis was performed. The of N$_2$ adsorption-desorption isotherms of porous-TiO$_2$, 2%WI and 5ALD are printed in Fig. 3. All of the three samples exhibit type III isotherms, indicating weak gas-solid interaction on the surface of photocatalysts [45]. Porous-TiO$_2$ display a type H2 hysteresis loop, demonstrating disordered pore size and shape. On the other hand, 2%WI and 5ALD samples show type H3 hysteresis loops, meaning slit-shaped pore shape [45]. It is likely that the added ALD-MgO layer stuffed on pore channels of porous-TiO$_2$ and narrowed the pore size. In Table 2, BET surface area and pore size of selected photocatalysts are listed.

BET surface area of porous-TiO$_2$ was measured to be 47.6 m^2/g, which is less than the value reported in the literature [23,24]. This likely is because a higher calcination temperature was used in this work to ensure removal of potential carbon residues from the synthesis

process, which on the other hand sintered the porous-TiO$_2$ porous structure. Nevertheless, porous-TiO$_2$ still exhibited comparable surface area to commercial P25 nanopowder (∼50 m^2/g). With addition of MgO, samples prepared by both WI and ALD methods showed increase in surface area at a very low MgO concentration (0.1%) or 1 ALD cycle MgO coating. It is possible that the addition of a trace amount of MgO or an ALD overlayer caused increased surface roughness at a length scale smaller than the crystal size of porous-TiO$_2$, thus increasing the surface area. While with a higher amount of MgO incorporation, pore channels in TiO$_2$ became stuffed with larger size MgO, leading to a decrease in surface area. The 10%WI sample had similar surface area to those of 2%WI sample and porous-TiO$_2$, indicating the morphology and nanostructure of MgO are similar to that of TiO$_2$. For the ALD samples, the surface area decreased more dramatically with the number of ALD cycles, and the 100ALD sample had a lower surface area than porous-TiO$_2$, possibly because the porous structure of porous-TiO$_2$ was smoothened by the denser ALD overlayer.

Pore size distributions of porous-TiO$_2$, 2%WI and 5ALD are also plotted in Fig. 3 based on BJH desorption data. Average pore sizes are listed in Table 2. A sharp peak centered at 5.7 nm was observed for porous-TiO$_2$, and the measured pores were likely a result of the spaces between the primary nanocrystals as observed from the TEM images in Fig. 2. Compared with porous-TiO$_2$, pores on of 2%WI expanded significantly, centered at ∼10 nm, ranging from ∼3.5 nm to ∼30 nm. All WI prepared samples showed expanded pore size, or larger inter-crystal spaces, which agrees with the TEM analysis in Fig. 2 that 2%WI sample
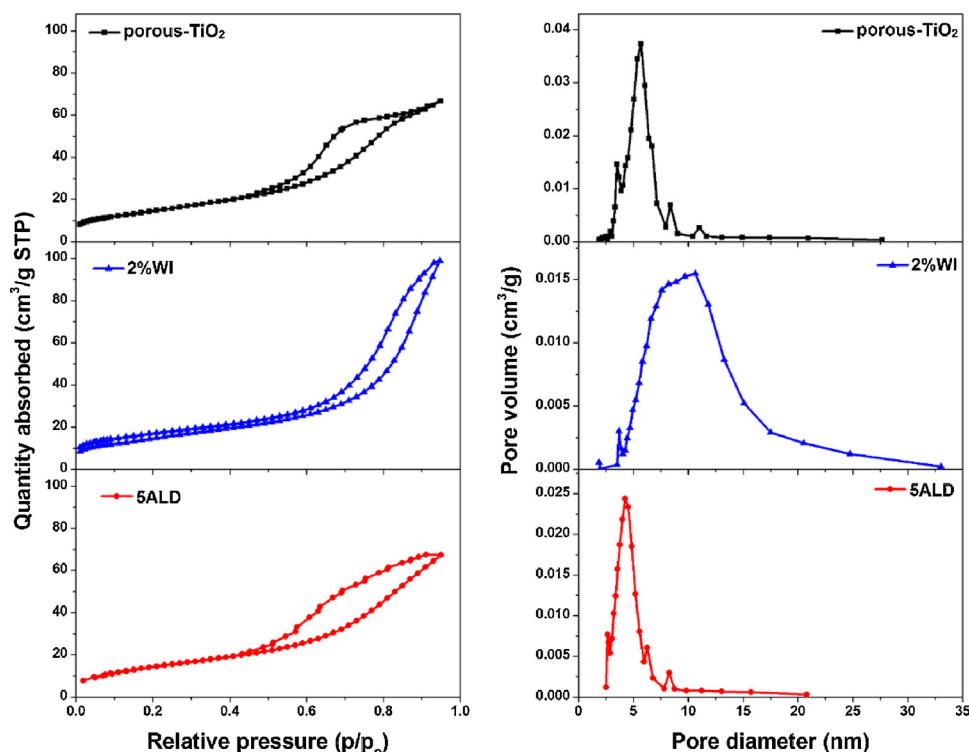
Fig. 3. N$_2$ adsorption-desorption isotherm (left) and pore size distribution (right) of porous-TiO$_2$, 2%WI and 5ALD.

Table 2
Surface area, average pore size, and band gap of representative photocatalysts.

Sample I.D.	BET surface area (m^2/g)	Average pore size (nm)	Band gap (eV)
porous-TiO$_2$	48	5.4	3.0
0.1%WI	62	6.0	3.0
2%WI	49	8.7	3.0
10%WI	49	7.7	3.1
1ALD	61	3.7	3.0
5ALD	52	4.4	3.0
100ALD	31	5.2	3.2

exhibited a loosened particle packing compared with porous-TiO$_2$. Similar to porous-TiO$_2$, 5ALD shows a sharp pore size distribution, but the peak slightly shifts towards lower pore size, centering at ~ 4.2 nm. For all three ALD prepared samples listed in Table 2, shrink in pore size was observed, which is reasonable because the ALD layer decreases the space in between the TiO$_2$ crystals.

3.4. Elemental analysis

To determine the chemical composition of prepared samples, EDS elemental mapping analysis was performed. Mg element was not detected on 2%WI and 5ALD from EDS mapping analysis, which is likely due to the very low amount of MgO. Thus, porous-TiO$_2$, 10%WI and 100ALD were used as representative samples in the EDS analysis, and the results are displayed in Fig. S6. As revealed by the EDS mapping, Ti was evenly distributed on all of the three samples; Mg was not detected on porous-TiO$_2$, but was uniformly dispersed on 10%WI and 100ALD, confirming successful deposition of MgO on the surface of 10%WI and 100ALD.

3.5. Photocatalyst surface analysis

Surface chemical states of representative samples were analyzed with X-ray photoelectron spectroscopy (XPS). XPS survey of porous-TiO$_2$, 2%WI and 5ALD samples can be found in Fig. S7. To confirm the presence of surface Mg, analysis on Mg *2p* peak was conducted. However, due to the low concentration of Mg and detection limit of the XPS instrument, Mg *2p* peak was only found on samples with higher amounts of Mg addition. Mg *2p* XPS spectra of 100ALD and 10%WI are printed in Fig. S8. Mg *2p* peaks found at ~ 50 eV confirm the existence of Mg element on both of the photocatalysts.

It has been reported that addition of MgO enables alternation of surface states on TiO$_2$ and promotes generation of defects such as Ti^{3+} and oxygen vacancy [41]. Ti^{3+} has been reported to improve the light absorption of TiO$_2$, hinder electron-hole recombination and improve photoactivity [7,46]. In addition, oxygen vacancies may serve as active sites in CO$_2$ photocatalytic reduction process [7,16]. However, oxygen vacancies are unstable and have a tendency to react with surface absorbed water and form surface hydroxyl groups (−OH), which also is another reactive species in CO$_2$ photoreduction by enhancing CO$_2$ adsorption and conversion [47]. Therefore, XPS was applied to study the chemical states of Ti (Ti^{3+} and Ti^{4+}) and O (surface hydroxyl bonded with Mg (Mg−OH) or Ti (Ti−OH) and lattice oxygen bonded with Mg (Mg−O) or Ti (Ti−O)), by analyzing Ti *2p* and O *1s* peaks. The Ti *2p* peaks in the photocatalyst are located at binding energies 458.7 eV (Ti^{4+} *2p$_{3/2}$*), 464.6 eV (Ti^{4+} *2p$_{1/2}$*), 457.7 eV (Ti^{3+} *2p$_{3/2}$*), and 463.4 eV (Ti^{3+} *2p$_{1/2}$*); while O *1s* peaks are located at binding energies 532.6 eV (Mg−OH), 530.5 eV (Mg−O), 531.9 eV (Ti−OH) and 529.9 eV (Ti−O) [41,48,49].

Deconvolution analyses of Ti *2p* spectra for porous-TiO$_2$, 2%WI and 5ALD are shown in Fig. 4. Surface Ti^{4+} and Ti^{3+} contents of selected samples are listed in Table 3. The surface of porous-TiO$_2$ is of 100% Ti^{4+} due to the process of calcination in air at a high temperature. On the surface of WI samples, a small fraction of Ti^{3+} was detected, and it increased with MgO concentration and became saturated at about 6.7% Ti^{3+} for 10%WI. As previously reported [41], introduction of MgO on surface of TiO$_2$ results in generation of surface Ti^{3+}, due to the interaction of Mg with surface TiO$_2$. For ALD coated samples, 5.4% of Ti^{3+} was detected with the addition of 1 layer of ALD coating, while it drastically increased to 12.0% and 30.3% for samples with 2 and 5 ALD
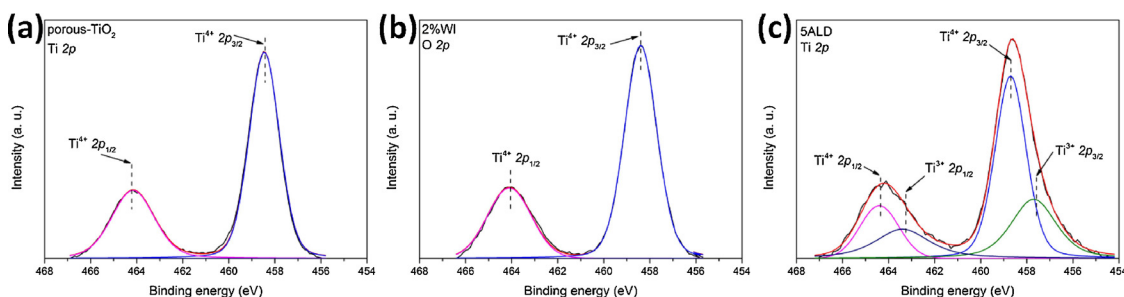
Fig. 4. Ti *2p* XPS spectra of (a) porous-TiO₂, (b) 2%WI, (c) 5ALD.

Table 3
Surface chemical states and their contents on the surface of photocatalyst samples.

Sample	Ti *2p* (%)		O *1s* (%)			
ID	Ti^{3+}	Ti^{4+}	Mg−OH	Mg−O	Ti−OH	Ti−O
porous-TiO₂	0.0	100.0	–	–	5.9	94.1
0.1%WI	0.7	99.3	0.6	20.0	5.0	74.4
1%WI	1.0	99.0	1.0	37.2	9.5	52.3
2%WI	2.6	97.4	3.2	40.3	7.0	49.5
5%WI	6.3	93.7	3.0	42.4	1.6	53.0
10%WI	6.7	93.3	3.0	44.1	2.9	50.0
1ALD	5.4	94.6	0.9	8.7	2.6	88.3
2ALD	12.0	88.0	1.0	10.2	2.3	86.5
5ALD	30.3	69.7	2.2	41.8	3.7	52.3
20ALD	N/A	N/A	8.3	84.5	0.0	7.2
100ALD	N/A	N/A	8.6	91.4	0.0	0.0

layers, respectively. This result clearly demonstrates a more significant impact of ALD coating than wet impregnation on the alternation of surface chemical states. For samples with 20 and 100 ALD layers, Ti peaks were hardly distinguishable from noises (Fig. S9) and thus were considered non-detectable. This is reasonable given the thicker coating of MgO masked X-ray exposure to the TiO₂ and XPS is sensitive only to a depth of a couple of nanometers on the surface. By comparing the Ti^{3+} percentage on the WI and ALD samples, it is clear that the extent of Mg species in generating/altering Ti surface states depends more on MgO coverage (by ALD) than on MgO loading amount (by WI).

Deconvolution analyses of O *1s* spectra for porous-TiO₂ and 2%WI and 5ALD are displayed in Fig. 5. The percentages of Ti−OH, Ti−O, Mg−OH and Mg−O based on the O *1s* analyses are calculated and listed in Table 3. On the surface of porous-TiO₂ sample, Ti−OH accounts for 5.9% of the surface species while the rest are Ti−O. The generation of small amount of surface OH groups is likely due to the adsorption of moisture from air. For WI samples, the percentages of surface Mg−OH and Mg−O have a positive correlation with MgO content in the range from 0.1% to 2% of MgO, while the percentages of total Ti coverage decreases, indicating an increased MgO surface coverage. From WI samples with larger than 2% MgO content, it is observed that the percentages of Mg−OH and Mg−O as well as those of Ti−OH and Ti−O

remain relatively constant. This implies that the MgO coverage on the WI catalyst surface reached a maximum value at around 2% MgO and further increasing the MgO content only caused aggregation of MgO particles rather than extending the coverage on the catalyst. For the ALD samples, the percentages of Mg−OH and Mg−O increased with the number of ALD layers in the range from 1 to 100 layers, while the Ti coverage decreased accordingly. When the number of ALD layers was more than 20, the catalyst surface was covered by almost all Mg species with minimal exposure of Ti species. These results again reveal the more significant impact on the surface coverage by the ALD method than by the WI method.

3.6. Photocurrent measurements

As shown in Fig. 6 under UV–vis irradiation, the photocurrent density of porous-TiO₂ was measured to be 2.0 μA/cm². With surface modification of MgO, the transient photocurrent density of 2%WI and 5ALD improved to 6.9 and 4.8 μA/cm², respectively, about 3.3 or 2.3 times as high as than that of porous-TiO₂. This result suggests the MgO modification improved photo-induced charge separation and transfer to the surface. The lower photocurrent generated on 5ALD than on 2%WI might be attributed to the more uniformly distributed MgO on the TiO₂ surface that adds more resistance to charge transfer.

3.7. Optical properties

The UV–vis diffuse reflectance spectra and band gap analyses are presented in Fig. S10. The band gap of porous-TiO₂ is measured at 3.0 eV, smaller than that of P25 (3.2 eV). The higher rutile phase percentage in porous-TiO₂ (56.1% rutile in porous-TiO₂ vs. ∼15% rutile in P25 [50]) is possibly responsible for the reduced band gap width. With addition of MgO species, no significant change in band gap and light absorption capacity was observed for both WI and ALD prepared samples, compared with that of porous-TiO₂. The band gap varied from 3.0 to 3.1 eV for WI samples. For ALD samples, the band gap of all samples except 100ALD was measured to be 3.0 eV; while 100ALD showed a slightly enlarged band gap value of 3.2 eV. It is possible that a thicker layer of MgO such as 100ALD may have changed the surface optical property. Overall, neither WI nor ALD modification caused significant changes in the optical properties of porous-TiO₂.
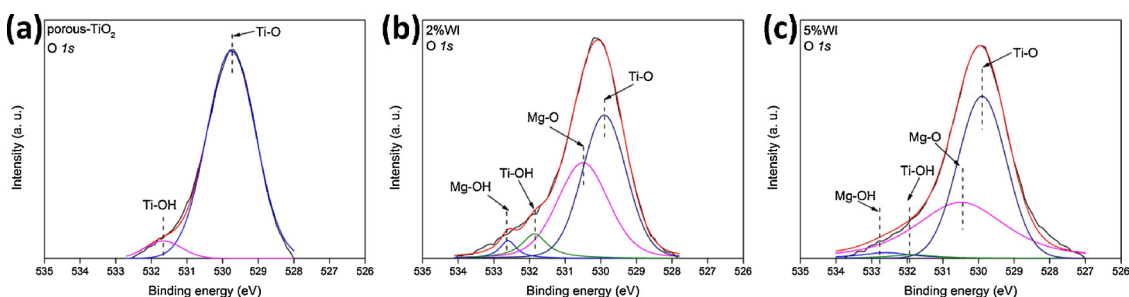

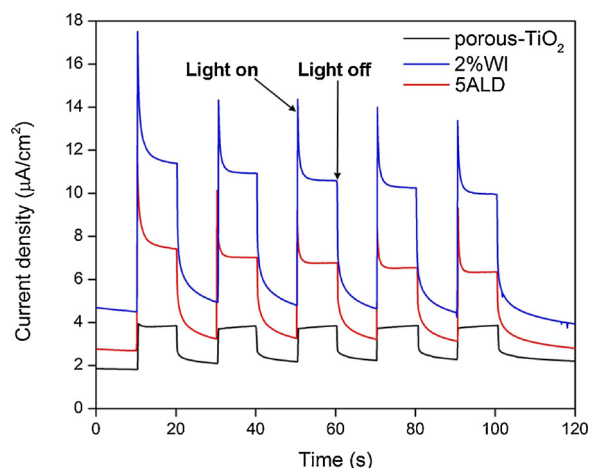**Fig. 5.** O *1s* XPS spectra of (a) porous-TiO₂, (b) 2%WI, (c) 5ALD.

Fig. 6. Transient photocurrent curves for porous-TiO_2, 2%WI, and 5ALD.
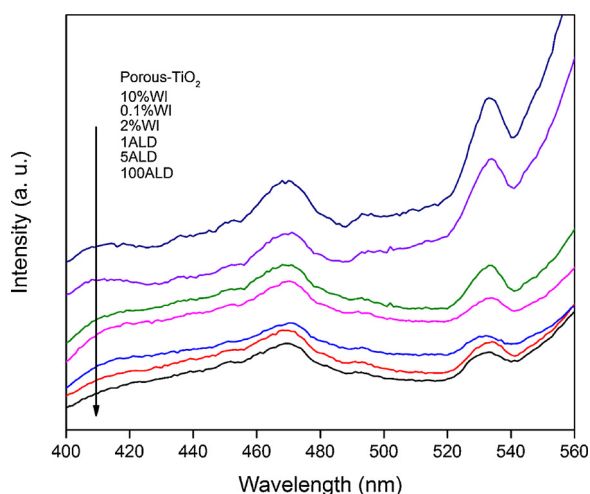

Fig. 7. Photoluminescence spectra of porous-TiO_2, WI and ALD samples.

To understand the surface electron-hole recombination characteristic of the prepared samples, photoluminescence spectra were measured. Since photoluminescence spectra record light emission generated by electron-hole recombination, quenched photoluminescence intensity indicates improved charge separation. As shown in Fig. 7, among the tested samples, porous-TiO_2 displayed the highest light emission, suggesting the largest surface recombination effect. Among WI samples, surface charge-hole recombination was suppressed with only 0.1% of

MgO addition, and 2%WI showed even weaker surface recombination effect. Reduction in photoluminescence suggests surface MgO played a key role in surface charge-hole separation. However, 10%WI showed higher photoluminescence than 0.1%WI, which suggests that excess MgO content on porous-TiO_2 surface might form recombination centers. For ALD prepared samples, with only 1 layer of MgO overcoating, the photoluminescence was significantly reduced compared with porous-TiO_2, the reduction in photoluminescence did not change much with more added ALD layers. Overall, the ALD samples showed lower photoluminescence intensity that the WI samples. This is likely due to the surface state passivation effect of ALD overcoating that hehp to reduce surface recombination. This mechanism was reported in our previously published work on CO_2 photoreduction by TiO_2 nanorods coated with an Al_2O_3 overlayer by ALD method [16].

3.8. CO_2 photoreduction performance under UV–vis irradiation

The CO_2 photoreduction tests were conducted with continuous flow of CO_2 and water vapor under UV–vis irradiation. The performances of WI and ALD samples in terms of CO production in comparison with P25 and porous-TiO_2 are shown in Fig. 8. It is necessary to mention that several blank tests were first conducted: (a) CO_2 + H_2O without photocatalysts under UV–vis irradiation; (b) CO_2 + H_2O with photocatalysts in the dark; (c) Ar + H_2O with photocatalysts under UV–vis irradiation. No carbon containing products were detected in those blank tests, indicating that the CO production reported in Fig. 8 was indeed derived from CO_2 reduction by the photocatalyst. In this study, CO was found to be the major product, while trace CH_4 production was found only on 2ALD, 5ALD and 10 ALD samples. No H_2 production was detected. Thus, only CO production was given and compared among the various catalysts. Commercially available P25 was used as a reference to demonstrate the improved performance of pristine and MgO modified porous-TiO_2. The CO produced by porous-TiO_2 (12.7 µmol/g) was 5.1-fold higher than that of P25 (2.5 µmol/g). Since porous-TiO_2 and P25 exhibited similar surface area (47.6 m^2/g for porous-TiO_2 vs. ~50 m^2/g for P25), the enhanced CO_2 photoreduction performance was attributed to the following two factors: (a) the porous hierarchical structure of porous-TiO_2; (b) the higher rutile to anatase ratio. The porous structure of porous-TiO_2 allows favorable intraparticle gas diffusion and facilitates gas diffusion and reactant-product exchange with the bulk, leading to relatively high reactant and low product concentrations around the surface of photocatalyst. In addition, according to previous reports [51–53], a phase weight ratio of 50–60% rutile in anatase/rutile mixed TiO_2 presents highly improved photocatalytic performance compared with TiO_2 with a higher anatase content. It is possible that the proper rutile percentage in porous-TiO_2 (~56%) contributes to the improved performance in CO_2 photocatalytic
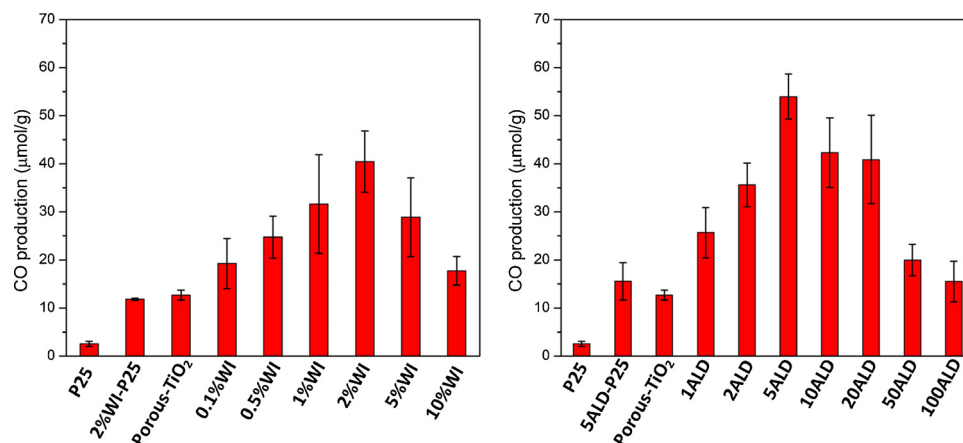

Fig. 8. CO production by (a) WI and (b) ALD samples during 4-h CO_2 photoreduction with water vapor.

reduction performance of porous-TiO_2 compared to P25.

With the modification of MgO, all WI samples and ALD samples displayed enhancement in photocatalytic CO_2 reduction performance. Due to the alkaline earth oxide nature of MgO, it is prone to generate surface hydroxyl even with the presence of trace amount of water vapor. The surface hydroxyl groups on MgO have higher basicity than those on TiO_2 that are slightly acidic [54]. For WI samples, the CO_2 photoreduction performance improved with MgO addition amount from 0.1% to 2%. Among all WI samples, the 2%WI sample presented the best photoreduction performance, 40.5 μmol/g, which is 3.2 times higher than porous-TiO_2 and 16.2 times higher than P25. The improvement of 2%WI compared with porous-TiO_2 is attributed to favorable properties originated from the MgO modification such as surface Ti^{3+} species and Mg−OH groups as seen in Table 3. However, too much amount of MgO addition on photocatalyst surface can reduce the contact of CO_2 molecule with TiO_2. In addition, the CO production is normalized by the total mass of TiO_2 and MgO, while TiO_2 is the only photo-active material. Increasing the MgO content above 5 wt. % did not increase the Ti^{3+} and Mg−OH significantly (Table 3) but reduced the amount of active TiO_2 content. As can be seen in Fig. 8a, with MgO percentage higher than 2%, CO_2 photoreduction performance started to drop.

The performance of CO_2 photoreduction by ALD samples are shown in Fig. 8b. The addition of a single atomic layer of MgO doubled the amount of CO production compared with pristine porous-TiO_2. The CO_2 photoreduction performance increased with the number of ALD layer from 1 to 5 layers and then decreased with more than 5 layers. The 5ALD sample was the optimum one among all ALD samples, producing 54.0 μmol/g CO, which was 4.3 times higher than porous-TiO_2 and 21.3 times higher than P25. With 30.3% surface Ti^{3+} concentration, 2.2% Mg−OH and 41.8% Mg-O concentration, it is reasonable that the 5ALD sample performed significantly better than porous-TiO_2, which had none of the above active species However, similar to WI samples, ALD samples with too "thick" a MgO overlayer (> 5 layers) experienced a decrease in CO_2 photoreduction performance. The decline in CO production can be attributed to the following reasons: (1) a decrease in surface area is observed with too many ALD layers, as seen in Table 2, which hinders the transport and adsorption of CO_2 in the porous TiO_2; and (2) an increase in the thickness of ALD overlayer increases the resistance for photoexcited electrons and holes to transfer to the surface of photocatalyst to initiate CO_2 reduction process. However, for catalysts with relatively "thick" layers such as 50ALD and 100ALD, the catalytic performance was not inferior to that of porous-TiO_2 thanks to the surface passivation effect of ALD layers that prevent surface charge recombination [16].

By comparing the photocurrent density data and CO_2 photoreduction performance of 2%WI and 5ALD, it was noticed that 2%WI showed higher photocurrent density but showed worse photocatalytic CO_2 performance compared to 5ALD. According to previously discussed, the major difference between 2%WI and 5ALD is the MgO morphology. Due to the nature of WI method, MgO are deposited on 2%WI as ultrafine nanoparticles, while MgO layer is more uniformly distributed on 5ALD. The difference in MgO morphology results variations in surface interaction with CO_2 molecules and thus affect CO_2 adsorption. The inconsistency in photocurrent density and overall CO_2 photoreduction performance and the difference in MgO morphology suggests better affinity of CO_2 with 5ALD over 2%WI. Because of high coverage on photocatalysts, 5ALD has more surface area to serve as absorbent to CO_2 molecules, as a result, photoexcited electrons can be more easily transferred to CO_2 molecules and thus the overall performance is improved.

In order to further demonstrate that porous-TiO_2 as a better candidate for photocatalytic CO_2 reduction applications over commercial P25, MgO modified P25 was prepared with 5 layers of MgO coating (denoted as 5ALD-P25) and 2% MgO of wet impregnation (denoted as 2%WI-P25). It was found that 2%WI-P25 produced 11.8 μmol/g of CO

(equivalent to 29.1% of that produced by 2%WI-porous-TiO_2), 5ALD-P25 sample produced 15.5 μmol/g of CO (equivalent to 28.7% of that produced by 5ALD-porous-TiO_2). Combining the result that P25 produced only 2.5 μmol/g of CO (equivalent to 19.2% of that produced by porous-TiO_2), it is apparent that porous-TiO_2 is advantageous over P25 no matter with or without MgO modification.

To investigate the effect of coating materials on the catalytic activity, we have conducted another experiment using ALD to coat 5 layers of Al_2O_3 on porous-TiO_2. The sample is denoted as 5ALD(Al_2O_3), and its catalytic activity is compared with that by 5ALD(MgO). The 5ALD(Al_2O_3) sample produced 19.2 μmol/g of CO, which is higher than the pristine porous-TiO_2 (12.7 μmol/g) but much lower than 5ALD (MgO) (54.0 μmol/g) as shown in Fig. 8. According to our previous report [16], an Al_2O_3_ALD overlayer on TiO_2 exhibits surface state preservation effect and thus promotes CO_2 photoreduction performance. This conclusion is once again confirmed in this work by comparing 5ALD(Al_2O_3) with porous-TiO_2. The difference in catalytic activity between 5ALD(Al_2O_3) and 5ALD(MgO) suggests that, in addition to surface state preservation effect, the MgO layer may promote adsorption of CO_2 due to a higher surface basicity. Because of the extremely trace amount of ALD coated MgO present on the surface, it was not possible to differentiate the equilibrium CO_2 adsorption capacity on the MgO-coated and Al_2O_3-coated or non-coated samples. Given that the 2%WI sample had 40.5 μmol/g CO production that is still much higher than the 5ALD(Al_2O_3) sample, it is likely the surface CO_2 adsorption enhancement due to MgO is one of the main reasons for the promoted CO_2 photoreduction activity, as also evidenced in our previous studies [22,23].

By comparing the best-performing ALD sample (5ALD) with the best-performing WI sample (2%WI), one can see that the performance of 5ALD in CO production was 28% better than that of 2%WI. The phase composition, surface area, crystal size, and band gap of 5ALD and 2%WI were similar (Table 2). The surface Mg atomic concentrations of the two samples were also very close (Table 3). The most extinct difference of the two materials is the surface Ti^{3+} concentration (30.3% on 5ALD and 2.6% on 2%WI), which may account for the better performance of 5ALD than 2%WI. This is because Ti^{3+} is usually paired with oxygen vacancies and those defect sites play a crucial role in facilitating charge transfer and separation as well as CO_2/H_2O adsorption and dissociation on the catalyst surface [7,18,46,55].

3.9. CO_2 photoreduction mechanism

With regard to the CO_2 photoreduction mechanism, it has been widely reported in the literature [56–58] that the formation of CO and CH_4 follows the two- and eight-electron reduction processes, respectively. It is reasonable that CO is found to be the major product in this work because much fewer electrons are needed to form CO than to form CH_4.

$$CO_2 + 2H^+ + 2e^- \rightarrow CO + H_2O \qquad (1)$$

$$CO_2 + 8H^+ + 8e^- \rightarrow CH_4 + 2H_2O \qquad (2)$$

Moreover, the surface oxygen vacancy/Ti^{3+} species is believed to improve CO_2 adsorption and activation on the surface, according to the following reactions, where CO_2^-, HCO_3^-, and CO_3^- species could be intermediate species for CO_2 reduction (Spontaneous dissociation of CO_2 to CO on defective surface of Cu (I)/TiO_{2-x} nanoparticles at room temperature [59].

$$Ti^{3+} + CO_2 \rightarrow Ti^{4+}-CO_2^- \qquad (3)$$

$$OH^- + CO_2 \rightarrow HCO_3^- \qquad (4)$$

$$Ti^{4+}-O^{2-} + CO_2 \rightarrow Ti^{4+}-CO_3^{2-} \qquad (5)$$

In this work, MgO modified on the TiO_2 surface, especially ALD-coated MgO significantly increased the surface Ti^{3+} and OH species,

and thus contributed to the production of CO_2 reduction intermediates as shown in Reactions ((3)–(5)). However, it is still not clear exactly how the MgO distribution and morphology affect the reaction pathways. This will be the direction of our future work.

4. Conclusion

This work for the first time applied ALD to effectively coat a thin, uniform layer of MgO on a MOF-derived porous TiO_2 photocatalyst and demonstrated significantly promoted CO_2 photoreduction performance, which was more than 4 times and 18 times higher than those of porous TiO_2 and commercial P25, respectively. A conventional wet-impregnation (WI) method was also applied to incorporate MgO on porous TiO_2 to compare against the ALD method. MgO modified catalysts prepared by both methods showed enhancement in CO production because of the added surface basicity to enhance CO_2 adsorption and the introduction of defect sites such as Ti^{3+} to promote electron-hole transfer. The ALD samples were advantageous over WI samples due to the generation of higher concentration of surface Ti^{3+} and the surface passivation effect of ALD coating that inhibits surface recombination. Material property analysis and photocatalytic activity results showed that ALD method is likely a better way for compared with conventional WI method with higher surface Ti^{3+} concentration, ALD coating surface state preservation effects as well as lower charge/hole recombination effects. The application of ALD as an enabling technique of surface modification to enhance catalytic performance successfully demonstrated in this work may be extended to catalysts beyond TiO_2 and to catalytic reactions beyond CO_2 reduction.

Acknowledgements

Appendix A. Supplementary data

Supplementary material related to this article can be found, in the online version, at doi:https://doi.org/10.1016/j.apcatb.2018.07.027.

References

[1] J. Qiao, Y. Liu, F. Hong, J. Zhang, A review of catalysts for the electroreduction of carbon dioxide to produce low-carbon fuels, Chem. Soc. Rev. 43 (2014) 631–675.

[2] W.-H. Wang, Y. Himeda, J.T. Muckerman, G.F. Manbeck, E. Fujita, CO_2 hydrogenation to formate and methanol as an alternative to photo- and electrochemical CO_2 reduction, Chem. Rev. 115 (2015) 12936–12973.

[3] M. Xing, F. Shen, B. Qiu, J. Zhang, Highly-dispersed boron-doped graphene nanosheets loaded with TiO_2 nanoparticles for enhancing CO_2 photoreduction, Sci. Rep. 4 (2014) 6341.

[4] S.N. Habisreutinger, L. Schmidt-Mende, J.K. Stolarczyk, Photocatalytic reduction of CO_2 on TiO_2 and other semiconductors, Angew. Chem. Int. Ed. 52 (2013) 7372–7408.

[5] K. Li, X. An, K.H. Park, M. Khraisheh, J. Tang, A critical review of CO_2 photoconversion: catalysts and reactors, Catal. Today 224 (2014) 3–12.

[6] L. Yuan, Y.-J. Xu, Photocatalytic conversion of CO_2 into value-added and renewable fuels, Appl. Surf. Sci. 342 (2015) 154–167.

[7] L. Liu, Y. Jiang, H. Zhao, J. Chen, J. Cheng, K. Yang, Y. Li, Engineering coexposed {001} and {101} facets in oxygen-deficient TiO_2 nanocrystals for enhanced CO_2 photoreduction under visible light, ACS Catal. 6 (2016) 1097–1108.

[8] W.-N. Wang, W.-J. An, B. Ramalingam, S. Mukherjee, D.M. Niedzwiedzki, S. Gangopadhyay, P. Biswas, Size and structure matter: enhanced CO_2 photoreduction efficiency by size-resolved ultrafine Pt nanoparticles on TiO_2 single crystals, J. Am. Chem. Soc. 134 (2012) 11276–11281.

[9] L. Liu, C. Zhao, J.T. Miller, Y. Li, Mechanistic study of CO_2 photoreduction with H_2O on Cu/TiO_2 nanocomposites by in situ X-ray absorption and infrared spectroscopies, J. Phys. Chem. C 121 (2017) 490–499.

[10] L. Liu, C. Zhao, J. Xu, Y. Li, Integrated CO_2 capture and photocatalytic conversion by a hybrid adsorbent/photocatalyst material, Appl. Catal. B: Environ. 179 (2015) 489–499.

[11] L. Zhang, W. Wang, D. Jiang, E. Gao, S. Sun, Photoreduction of CO_2 on BiOCl nanoplates with the assistance of photoinduced oxygen vacancies, Nano Res. 8 (2015) 821–831.

[12] C.-C. Lo, C.-H. Hung, C.-S. Yuan, J.-F. Wu, Photoreduction of carbon dioxide with H_2 and H_2O over TiO_2 and ZrO_2 in a circulated photocatalytic reactor, Sol. Energy Mater. Sol. Cells 91 (2007) 1765–1774.

[13] A. Crake, K.C. Christoforidis, A. Kafizas, S. Zafeiratos, C. Petit, CO_2 capture and photocatalytic reduction using bifunctional TiO_2/MOF nanocomposites under UV–vis irradiation, Appl. Catal. B: Environ. 210 (2017) 131–140.

[14] M. Wang, D. Wang, Z. Li, Self-assembly of CPO-27-Mg/TiO_2 nanocomposite with enhanced performance for photocatalytic CO_2 reduction, Appl. Catal. B: Environ. 183 (2016) 47–52.

[15] X. Xiang, F. Pan, Y. Li, A review on adsorption-enhanced photoreduction of carbon dioxide by nanocomposite materials, Adv. Compos. Hybrid Mater. 1 (2018) 6–31.

[16] H. Zhao, J. Chen, G. Rao, W. Deng, Y. Li, Enhancing photocatalytic CO_2 reduction by coating an ultrathin Al_2O_3 layer on oxygen deficient TiO_2 nanorods through atomic layer deposition, Appl. Surf. Sci. 404 (2017) 49–56.

[17] O. Ola, M.M. Maroto-Valer, Review of material design and reactor engineering on TiO_2 photocatalysis for CO_2 reduction, J. Photochem. Photobiol. C: Photochem. Rev. 24 (2015) 16–42.

[18] H. Zhao, F. Pan, Y. Li, A review on the effects of TiO_2 surface point defects on CO_2 photoreduction with H_2O, J. Materiom. 3 (2017) 17–32.

[19] A. Nikokavoura, C. Trapalis, Alternative photocatalysts to TiO_2 for the photocatalytic reduction of CO_2, Appl. Surf. Sci. 391 (2017) 149–174.

[20] H. Li, M. Eddaoudi, M. O'Keeffe, O.M. Yaghi, Design and synthesis of an exceptionally stable and highly porous metal-organic framework, Nature 402 (1999) 276–279.

[21] X. Xu, R. Cao, S. Jeong, J. Cho, Spindle-like mesoporous α-Fe_2O_3 anode material prepared from MOF template for high-rate lithium batteries, Nano Lett. 12 (2012) 4988–4991.

[22] Z. Xie, C. Jiang, W. Xu, X. Cui, C. de los Reyes, A.A. Martí, Y. Wang, Facile self-assembly route to Co_3O_4 nanoparticles confined into single-walled carbon nanotube matrix for highly reversible lithium storage, Electrochim. Acta 235 (2017) 613–622.

[23] Z. Wang, X. Li, H. Xu, Y. Yang, Y. Cui, H. Pan, Z. Wang, B. Chen, G. Qian, Porous anatase TiO_2 constructed from a metal-organic framework for advanced lithium-ion battery anodes, J. Mater. Chem. A 2 (2014) 12571–12575.

[24] W.-W. Zhan, Q.-L. Zhu, S. Dang, Z. Liu, M. Kitta, K. Suenaga, L.-S. Zheng, Q. Xu, Synthesis of highly active sub-nanometer Pt@Rh core–shell nanocatalyst via a photochemical route: porous titania nanoplates as a superior photoactive support, Small (2017) 1603879–1603879.

[25] Y.-N. Li, Z.-Y. Chen, S.-J. Bao, M.-Q. Wang, C.-L. Song, S. Pu, D. Long, Ultrafine TiO_2 encapsulated in nitrogen-doped porous carbon framework for photocatalytic degradation of ammonia gas, Chem. Eng. J. 331 (2018) 383–388.

[26] R. Tang, R. Yin, S. Zhou, T. Ge, Z. Yuan, L. Zhang, L. Yin, Layered MoS_2 coupled MOFs-derived dual-phase TiO_2 for enhanced photoelectrochemical performance, J. Mater. Chem. A 5 (2017) 4962–4971.

[27] Z. Guo, J.K. Cheng, Z. Hu, M. Zhang, Q. Xu, Z. Kang, D. Zhao, Metal-organic frameworks (MOFs) as precursors towards TiO_x/C composites for photodegradation of organic dye, RSC Adv. 4 (2014) 34221–34225.

[28] H. Li, X. Wu, J. Wang, Y. Gao, L. Li, K. Shih, Enhanced activity of AgMgOTiO_2 catalyst for photocatalytic conversion of CO_2 and H_2O into CH_4, Int. J. Hydrogen Energy 41 (2016) 8479–8488.

[29] Z. Xiong, Z. Lei, C.-C. Kuang, X. Chen, B. Gong, Y. Zhao, J. Zhang, C. Zheng, J.C.S. Wu, Selective photocatalytic reduction of CO_2 into CH_4 over Pt-Cu_2O TiO_2 nanocrystals: the interaction between Pt and Cu_2O cocatalysts, Appl. Catal. B: Environ. 202 (2017) 695–703.

[30] G. Rao, H. Zhao, J. Chen, W. Deng, B. Jung, A. Abdel-Wahab, B. Batchelor, Y. Li, FeOOH and Fe_2O_3 co-grafted TiO_2 photocatalysts for bisphenol A degradation in water, Catal. Commun. 97 (2017) 125–129.

[31] C.G. Morales-Guio, M.T. Mayer, A. Yella, S.D. Tilley, M. Grätzel, X. Hu, An optically transparent iron nickel oxide catalyst for solar water splitting, J. Am. Chem. Soc. 137 (2015) 9927–9936.

[32] H. Irie, K. Kamiya, T. Shibanuma, S. Miura, D.A. Tryk, T. Yokoyama, K. Hashimoto, Visible light-sensitive Cu(II)-grafted TiO_2 photocatalysts: activities and X-ray absorption fine structure analyses, J. Phys. Chem. C 113 (2009) 10761–10766.

[33] J. Low, B. Cheng, J. Yu, Surface modification and enhanced photocatalytic CO_2 reduction performance of TiO_2: a review, Appl. Surf. Sci. 392 (2017) 658–686.

[34] F. Xu, J. Zhang, B. Zhu, J. Yu, J. Xu, $CuInS_2$ sensitized TiO_2 hybrid nanofibers for improved photocatalytic CO_2 reduction, Appl. Catal. B: Environ. 230 (2018) 194–202.

[35] S. Bai, W. Yin, L. Wang, Z. Li, Y. Xiong, Surface and interface design in cocatalysts for photocatalytic water splitting and CO_2 reduction, RSC Adv. 6 (2016) 57446–57463.

[36] L. Liu, C. Zhao, D. Pitts, H. Zhao, Y. Li, CO_2 photoreduction with H_2O vapor by porous MgO-TiO_2 microspheres: effects of surface MgO dispersion and CO_2 adsorption-desorption dynamics, Catal. Sci. Technol. 4 (2014) 1539–1546.

[37] L. Liu, C. Zhao, H. Zhao, D. Pitts, Y. Li, Porous microspheres of MgO-patched TiO_2 for CO_2 photoreduction with H_2O vapor: temperature-dependent activity and stability, Chem. Commun. 49 (2013) 3664–3666.

[38] F. Wang, Y. Zhou, P. Li, L. Kuai, Z. Zou, Synthesis of bionic-macro/microporous MgO-modified TiO_2 for enhanced CO_2 photoreduction into hydrocarbon fuels, Chin. J. Catal. 37 (2016) 863–868.

[39] S. Kwon, P. Liao, P.C. Stair, R.Q. Snurr, Alkaline-earth metal-oxide overlayers on TiO_2: application toward CO_2 photoreduction, Catal. Sci. Technol. 6 (2016) 7885–7895.

[40] Q. Li, L. Zong, C. Li, J. Yang, Photocatalytic reduction of CO_2 on MgO/TiO_2

nanotube films, Appl. Surf. Sci. 314 (2014) 458–463.

[41] M. Manzanares, C. Fàbrega, J. Oriol Ossó, L.F. Vega, T. Andreu, J.R. Morante, Engineering the TiO_2 outermost layers using magnesium for carbon dioxide photoreduction, Appl. Catal. B: Environ. 150–151 (2014) 57–62.

[42] X. Yuan, H. Wang, Y. Wu, G. Zeng, X. Chen, L. Leng, Z. Wu, H. Li, One-pot self-assembly and photoreduction synthesis of silver nanoparticle-decorated reduced graphene oxide/MIL-125(Ti) photocatalyst with improved visible light photocatalytic activity, Appl. Organomet. Chem. 30 (2016) 289–296.

[43] H. Rietveld, A profile refinement method for nuclear and magnetic structures, J. Appl. Crystallogr. 2 (1969) 65–71.

[44] R. Jin, W. Gao, J. Chen, H. Zeng, F. Zhang, Z. Liu, N. Guan, Photocatalytic reduction of nitrate ion in drinking water by using metal-loaded $MgTiO_3$-TiO_2 composite semiconductor catalyst, J. Photochem. Photobiol. A: Chem. 162 (2004) 585–590.

[45] Z. ALOthman, A review: fundamental aspects of silicate mesoporous materials, Materials 5 (2012) 2874.

[46] L. Liu, Y. Li, Understanding the reaction mechanism of photocatalytic reduction of CO_2 with H_2O on TiO_2-based photocatalysts: a review, Aerosol Air Qual. Res. 14 (2014) 453–469.

[47] H. Yu, S. Yan, P. Zhou, Z. Zou, CO_2 photoreduction on hydroxyl-group-rich mesoporous single crystal TiO_2, Appl. Surf. Sci. 427 (2018) 603–607.

[48] F. El-Gohary, A. Tawfik, U. Mahmoud, Comparative study between chemical coagulation/precipitation (C/P) versus coagulation/dissolved air flotation (C/DAF) for pre-treatment of personal care products (PCPs) wastewater, Desalination 252 (2010) 106–112.

[49] B. Erdem, R.A. Hunsicker, G.W. Simmons, E.D. Sudol, V.L. Dimonie, M.S. El-Aasser, XPS and FTIR surface characterization of TiO_2 particles used in polymer encapsulation, Langmuir 17 (2001) 2664–2669.

[50] B. Ohtani, O.O. Prieto-Mahaney, D. Li, R. Abe, What is Degussa (Evonik) P25?

Crystalline composition analysis, reconstruction from isolated pure particles and photocatalytic activity test, J. Photochem. Photobiol. A: Chem. 216 (2010) 179–182.

[51] M. Yan, F. Chen, J. Zhang, M. Anpo, Preparation of controllable crystalline titania and study on the photocatalytic properties, J. Phys. Chem. B 109 (2005) 8673–8678.

[52] S. Bakardjieva, J. Šubrt, V. Štengl, M.J. Dianez, M.J. Sayagues, Photoactivity of anatase–rutile TiO_2 nanocrystalline mixtures obtained by heat treatment of homogeneously precipitated anatase, Appl. Catal. B: Environ. 58 (2005) 193–202.

[53] T. Ohno, K. Tokieda, S. Higashida, M. Matsumura, Synergism between rutile and anatase TiO_2 particles in photocatalytic oxidation of naphthalene, Appl. Catal. A: Gen. 244 (2003) 383–391.

[54] H. Onishi, T. Aruga, C. Egawa, Y. Iwasawa, Adsorption of CH_3OH, $HCOOH$ and SO_2 on TiO_2(110) and stepped TiO_2(441) surfaces, Surf. Sci. 193 (1988) 33–46.

[55] X. Xin, T. Xu, J. Yin, L. Wang, C. Wang, Management on the location and concentration of Ti^{3+} in anatase TiO_2 for defects-induced visible-light photocatalysis, Appl. Catal. B: Environ. 176–177 (2015) 354–362.

[56] E. Karamian, S. Sharifnia, On the general mechanism of photocatalytic reduction of CO_2, J. CO_2 Util. 16 (2016) 194–203.

[57] S.S. Tan, L. Zou, E. Hu, Kinetic modelling for photosynthesis of hydrogen and methane through catalytic reduction of carbon dioxide with water vapour, Catal. Today 131 (2008) 125–129.

[58] L.O. Kamila Kočí, Olga Šolcová, Kinetic study of photocatalytic reduction of CO_2 over TiO_2, Chem. Process Eng. 31 (2010) 395–407.

[59] L. Liu, C. Zhao, Y. Li, Spontaneous dissociation of CO_2 to CO on defective surface of $Cu(I)/TiO_{2-x}$ nanoparticles at room temperature, J. Phys. Chem. C 116 (2012) 7904–7912.